Biosensors and Bioelectronics 137 (2019) 8–14

Contents lists available at ScienceDirect

Biosensors and Bioelectronics

journal homepage: www.elsevier.com/locate/bios

High-resolution separation of DNA/proteins through nanorod sieving matrix

Zhen Cao[a], Yu Zhu[b], Yang Liu[a], Shurong Dong[a], Jiongdong Zhao[a], Ye Wang[a], Shu Yang[c,**], Junxue Fu[d,*]

[a] College of Information Science and Electronic Engineering, Zhejiang University, Hangzhou, 310027, PR China
[b] Suzhou Institute of Nano-tech and Nano-Bionics, Chinese Academy of Sciences, Suzhou, 215123, PR China
[c] College of Electrical Engineering, Zhejiang University, Hangzhou, 310027, PR China
[d] Department of Physics, Hong Kong Baptist University, Kowloon Tong, Hong Kong S. A. R, PR China

ARTICLE INFO

Keywords:
DNA
Proteins
Separation
Nanofluidics
Localized oblique angle deposition

ABSTRACT

In this paper, we report on an integrated nanorod array as a novel sieving matrix for high-resolution separation of biomolecules. A wide size range of DNA (100 bp–166 kbp) and proteins (11.4 kDa–205 kDa) are resolved into sharp peaks within several minutes using devices with various pore apertures, either in a reptation mode or Ogston mechanism. The device delivers notable performance with the minimum resolvable size difference 10 bp for 100 bp and 150 bp DNA fragments, 15.9 kbp for 48 kbp and 166 kbp DNA chains, and 7.9 kDa for 11.4 and 68 kDa proteins, where the separation efficiency is higher than or comparable to other micro/nanofabricated artificial sieving structures. The process utilizes localized oblique angle deposition (LOAD) to simply integrate densely packed nanorods onto steep sidewalls of microfluidic channels, which eliminates the requirement of advanced lithography tools routinely used in conventional artificial sieving structures. We further demonstrate the modulation of pore aperture that employs the sculptured sidewalls by a custom deep reactive-ion etching (DRIE) recipe. Given the easy fabrication, excellent engineering control and outstanding sieving capability, this nanorod sieve device has great potentials to provide a simple and effective separation technique for biomolecule analysis.

1. Introduction

The ability to effectively and sensitively separate DNA or proteins is of utmost importance in bioanalysis and biomedical engineering (Lee et al., 2016; Ma et al., 2011; Smejkal and Lazarev, 2006; Westermeier, 2016). Over the years, gel electrophoresis remains the most commonly used method for sizing DNA or protein mixtures. The random pores in gel interact with biomolecules that pass through and fractionalize them to an extent that is commensurate with their size (Liu et al., 1992; Stellwagen, 2009; Viovy and Duke, 1993). However, these gel slabs have intrinsic difficulties for the incorporation into confining spaces of microchips. Moreover, the gelatinous gel slabs require several hours for preparation which is time consuming and labor intensive. The performance even deteriorates severely when separating long DNA molecules (> 20 kbp) under a DC electric field (Viovy, 2000). To surmount these limitations, much interest has been switched to micro/nanochip systems which utilize microfabrication to pattern ordered filtering structures for DNA and protein fractionation (Dorfman, 2010; Fu et al., 2008). These so-called artificial gel structures allow for more rigorous separation and provide insights into the fundamental physics of electrophoresis.

The first artificial sieving structure by Volkmuth and Austin reported size-dependent electrophoretic behaviors of long DNA molecules using silicon post arrays (Volkmuth and Austin, 1992). This revolutionary work opens up new opportunities for highly sensitive separation of DNA and proteins through micro/nanofabricated molecular sieves. Periodic arrays of micro/nanopillars were constructed through optical (Bakajin et al., 2001; Huang et al., 2002) or e-beam lithography (Baba et al., 2003; Kaji et al., 2004). Long DNA molecules were sorted according to their sizes via the DNA-post collisions, either in a batch (Huang et al., 2002) or a continuous operation (Baba et al., 2003; Bakajin et al., 2001; Kaji et al., 2004). Alternatively, microchannels with alternating segments of deep and shallow wells were proposed for their extremely high resolving power on the basis of entropic barriers at slit-well interfaces (Fu et al., 2005, 2006; Han et al., 1999; Han and Craighead, 1999, 2000, 2002). These energy barriers can be categorized as a conformational type for sorting long DNA molecules (the entropic-trapping regime) (Han et al., 1999; Han and Craighead, 1999, 2000,

* Corresponding author.
** Corresponding author.
E-mail addresses: eesyang@zju.edu.cn (S. Yang), phyjxfu@hkbu.edu.hk (J. Fu).

https://doi.org/10.1016/j.bios.2019.04.033
Received 24 February 2019; Received in revised form 15 April 2019; Accepted 17 April 2019
Available online 20 April 2019
0956-5663/

2002), and a configurational type for sieving short DNA molecules and proteins (Ogston sieving) (Fu et al., 2005, 2006). Cao et al. replaced these slits with highly regular integrated capillaries for fast sieving of DNA and proteins within several minutes under large field strength (Cao and Yobas, 2014, 2015). More recently, nanoscale deterministic lateral displacement (nanoDLD) devices were fabricated using e-beam and deep-ultraviolet (DUV) lithography and applied for continuous fractionation of small biomolecules (Wunsch et al., 2016, 2019; Zeming et al., 2018). Other typical micro/nanochip systems utilized asymmetric obstacle courses (Duke and Austin, 1998; Huang et al., 2003), three-dimensional nanowire (Rahong et al., 2015) or nanowall arrays as the artificial sieving matrix (Yasui et al., 2011). Nevertheless, almost all the aforementioned structures heavily rely upon high-resolution lithography tools, resulting in high cost and low throughput. Moreover, the separation of various biomolecules requires different constriction sizes of the devices that are comparable to the molecular diameter. However, the flexibility of pore aperture is limited by expensive mask or mold modification and cumbersome process development. Besides, bare narrow open capillaries were used to resolve a wide size-range of DNA fragments with hydrodynamic chromatography. While high separation efficiency of more than a million plates per meter was achieved, complicated pressure generation apparatus was usually involved (Wang et al., 2008, 2010; Zhu et al., 2013). Gao et al. demonstrated label-free and sensitive electrochemical sensors for femtomolar DNA detection and methylation quantification (Gao et al., 2017, 2018). Surface enhanced Raman spectroscopy for DNA detection was also reported using silver nanoparticles (Qian et al., 2018).

In this work, we propose a unique sieving matrix, which consists of dense nanorod arrays embedded on the sidewalls of microchannels for gel-free fractionation of DNA and proteins. These extruded nanorods can be envisioned as an array of obstacles and interact with biomolecules as they pass through under a dc voltage. Distinct mixtures of DNA and proteins finally get resolved into sharp peaks according to their molecular weights. Compared with conventional artificial sieving structures such as pillar/post arrays, asymmetric obstacle courses or slit-well motifs, the process here adopts localized oblique angle deposition (LOAD) (Fu et al., 2011; Ji et al., 2016; Zhang et al., 2013) which easily integrates dense arrays of nanorods on pre-structured channels through a simple shadowing-based deposition. This method of fabrication differs from previous methods of constructing nanoscale channels for sieving biomolecules, which usually require advanced lithography tools (*e.g.*, e-beam lithography, nanoimprint) or meticulous wafer bonding techniques. More importantly, the scaling of critical pore aperture down to sub-100 nm progresses through a custom deep reactive ion etch (DRIE) process. Here, this tunable sieving matrix is incorporated into microfluidic chips for biomolecule separation over a broad size scope. We demonstrate separation of long DNA, short DNA and proteins, with the minimum resolvable size difference 10 bp for 100 bp and 150 bp DNA fragments, 15.9 kbp for 48 kbp and 166 kbp DNA chains, and 7.9 kDa for 11.4 and 68 kDa proteins. The separation resolution achieved is comparable to or relatively higher than the state-of-the-art. This is attributed to the dense pack of nanorods which create more constrictions and greater entropic barriers on molecules than less resistive submicrometer pillars or slits do.

The conceptual illustration of the artificial sieving matrix investigated here is shown in Fig. 1A. The device engages a paradigm commonly used in chip-based capillary electrophoresis, which consists of a sample injection cross-junction and a separation channel packed with nanorod arrays. A pinched plug of biological sample is electrokinetically injected from the loading channel into the sieving matrix. The constituent molecules encounter various retarding forces as they migrate through these confining spaces (Fig. 1A, inset), resulting in size-dependent electrophoretic separation at the end of detection channel. Nanorods acting as the sieving matrix are deposited onto sidewalls of the separation channel through LOAD. Fig. 1B illustrates the principle of nanorod growth and pore formation through LOAD process. In the beginning of deposition, vapor atoms form nuclei with different heights on the surface. Due to a very large deposition angle θ ($> 75^{\circ}$), *i.e.* the angle between incident vapor and surface normal, short nuclei will be shadowed by the taller ones and thus stop growing. The porosity of the nanorod film is determined by the deposition angle and the relative height difference between adjacent nuclei. In this work, the incident vapor and sidewall of separation channel naturally form a large deposition angle, when the device is horizontally mounted in the deposition chamber, as shown in Fig. 1C and D. A custom DRIE process is employed to delicately modulate the surface roughness of sidewalls. One can expect that a sculptured sidewall produces a low porosity matrix (Fig. 1C), while a “smooth” sidewall will result in a high porosity sieving matrix (Fig. 1D). The device proposed here possesses the sieving capability for a wide range of biomolecules due to the flexibility of the porosity of these nanorods. The resolution achieved is significantly high, mainly because the steep entropic barriers created by these nanorod arrays largely alleviate the diffusion of the sample band.

2. Material and methods

2.1. Device fabrication

The fabrication of our artificial sieving device started from p-type, (100)-oriented silicon wafers (thickness 525 μm). The wafers were patterned with the sample injection cross-junction (20 μm wide, 3 μm deep) and the separation channels (3 μm wide, 3 μm deep) through conventional lithography and a DRIE step. The structured wafers were then electrically passivated through a layer of thermally grown 1-μm thick silicon oxide. After being covered by a deposition mask, the substrates were placed on a leveled stage of an e-beam evaporator and pumped to a vacuum of 10^{-6} Torr. The deposition rates and film thicknesses were monitored by a quartz crystal microbalance (QCM). A 5-nm thin film of titanium was firstly deposited at a rate of 2 Å/s as adhesive layer. The nanorods were consecutively integrated into the separation channels through a deposition of 5-μm thick silicon dioxide at a rate of 4 Å/s. The steep sidewalls of the channels, slightly slanted with respect to the surface normal, readily offered an ideal deposition angle for shadowing effect. It is noted that the sculptured edges on sidewalls become isolated sites for preferential growth of nanostructures by shadowing the region behind them (Fig. 1C). Therefore the porosity of these nanorods can be easily controlled and precisely defined through a custom DRIE recipe, which consists of alternatively repeating two modes, etching and passivation. To achieve nanorod array sieves with 200-nm pore aperture, we utilized 8 successive DRIE cycles, each consisting 7 s etch (C_4F_8 15 sccm, SF_6 45 sccm, O_2 5 sccm) and 5.2 s passivation (C_4F_8 75 sccm). These regular indentations etched on sidewalls created the shadowing effect during deposition and subsequently form the sieving matrix. To reduce the pore aperture for sieving small DNA and proteins, we simultaneously conducted etching and passivation cycle for 8 min. As a result, channels with smooth sidewalls were structured on wafers for the further formation of nanorod array sieve with sub-100 nm pore aperture (Fig. 1D). Defects could be observed at the bottom of the channels due to the uneven etching profile at the corners, as can be seen in Fig. 1D. However, the separation results are unaffected as only a small quantity of molecules will pass through these apertures under high lateral electric fields.

2.2. Reagents

The double-stranded DNA molecules, including bacteriophage lambda cI857 Sam 7 (λDNA, 48 kbp) and 100 bp DNA ladder, were purchased from Sigma-Aldrich. The bacteriophage T4 GT7 DNA (166 kbp) was obtained from Nippon Gene. All the DNA was stained with intercalating dye YOYO-1 at a dye/base pair ratio of 1:10 and diluted to a final concentration of 50 μg/mL in 5 × TBE buffer (450 mM Tris/borate, 10 mM EDTA, pH 8.3). 4% v/v 2-mercaptoethanol and 1% v/v

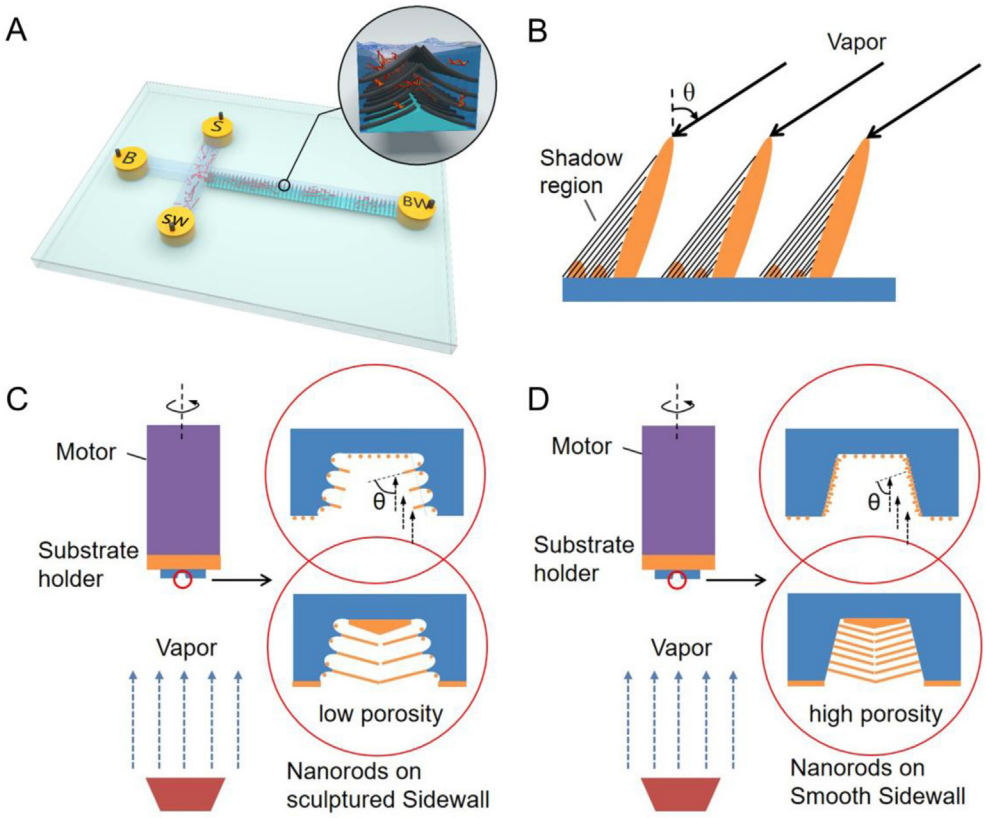

Fig. 1. (A) Conceptual illustration of the artificial sieving device integrated with nanorod arrays for biomolecule separation. The nanorods grow on the steep wall of the trench through localized oblique angle deposition (LOAD) and create a robust three dimensional nanofluidic sieve in the separation channel. The device also integrates a sample injection cross with reservoirs assigned as buffer (B), buffer waste (BW), sample (S), and sample waste (SW). The plug of DNA or protein mixture is injected and resolved into distinct peaks due to the interaction with the nanorods. (B) During deposition, vapor atoms arrive and nucleate growth sites on the surface. The uneven heights of nuclei eventually lead to the growth of voids due to the shadowing effect. The degree of porosity is determined by the deposition angle θ and the roughness of the surface. (C, D) The schematics show the growth of (C) low porosity nanorods on sculptured sidewalls and (D) high porosity nanorods on smooth sidewalls through LOAD.

poly-(vinylpyrrolidone) (MW = 10000) were added to reduce photobleaching and suppress electro-osmosis of the channel. Six proteins conjugated with Alexa Fluor 488, including cholera toxin subunit B (11.4 kDa), bovine serum albumin (BSA, 68 kDa), lectin GS-II (Griffonia simplicifolia, 113 kDa), β-galactosidase (116 kDa), human low-density lipoprotein (179 kDa) and myosin (205 kDa), were purchased from Life technologies. These proteins were denatured by mixing with 2 wt % SDS (Sigma-Aldrich) and 0.1 M dithiothreitol (DTT, Sigma-Aldrich). The mixture was treated in an 80 °C water bath for 20 min incubation and diluted with 5 × TBE buffer to a final concentration of 0.1 mg/mL.

2.3. Experiments

The device was aligned and bonded with a plain poly (dimethylsiloxane) (PDMS; Dow Corning 184) slab bored with four inlet/outlet ports upon activating their surfaces in oxygen plasma (29.6 W, 45 s, Harrick Plasma). For the electrokinetic injection and separation, four platinum electrodes were immersed into the reservoirs and controlled by a high voltage power supply module (Tianjin Dongwen Co., Ltd, China) using LABVIEW software (National Instruments). The device under test was observed through an epi-fluorescence microscope (FN1; Nikon, Japan) equipped with a solid-state laser at 488 nm and the filter cube for fluorescent detection (Ex/Em 492/520 nm). Time-series images were captured using an EMCCD camera (iXon3 897, Andor). The fluorescent intensity was analyzed by an image processing software (ImageJ; NIH, Bethesda) to generate electropherograms.

3. Results and discussion

3.1. Sieve structure

The porosity of the nanorod sieve plays a decisive role in separation range and sieving mechanism of biomolecules. To achieve various porosities of sieving structures, we utilize a modified DRIE process to create the microchannels on the wafers prior to the deposition. The steep sidewalls of these channels are slanted with respect to the wafer surface normal by 7°, therefore allowing LOAD without tilting the substrate. Besides, the undulating sidewalls imparted by repeating isotropic etching and passivation provide an appropriate roughness for shadowing effect and subsequent growth of nanorods. Fig. 2A shows the cross-sectional view of microchannels from a representative device prior to the deposition. A repeating pattern of 10 trenches constitutes the separation channel with all trenches 3 μm wide and 3 μm deep. The inset reveals the detailed channel profile with a steep sidewall and sculptured edges. These taper scallops are measured with an average size of 200 nm, on which nanorods grow up and fill in the entire channel space after deposition, as depicted in Fig. 2B. The DRIE process prescribed here is also revised for a smooth sidewall as shown in Fig. 2C. The inset reveals the close-up view of the channel profile, which is found to be free of the previous undulating roughness and still keep a 7° sidewall angle. The resultant nanorods are densely packed inside the trench with sub-100 nm aperture, which is suitable for the sieving of small DNA and proteins.

We also investigated the fabrication variability across the devices and batches. From the same batch, we randomly cut the separation channels of ten devices and evaluated their cross-section from scanning electron microscopy (SEM) images. For 200-nm and sub-100 nm sieve devices, the aperture between nanorods yielded values of 201.1 ± 26.9 and 74.8 ± 14.3 nm, respectively. The mean and standard deviation values were obtained by measuring the gaps of channels from ten different devices. We also evaluated the devices from another two batches yielded values of 194.3 ± 34.5, 209.1 ± 37.8 nm in one batch and 72.8 ± 9.2, 71.2 ± 10.4 nm in another, respectively. The uniformity within wafers and across batches was generally less than 20%. The non-consistency was mainly attributed to the etching variations and the induced non-uniform sidewall profile. Investigations are currently underway to reduce the fabrication variations.

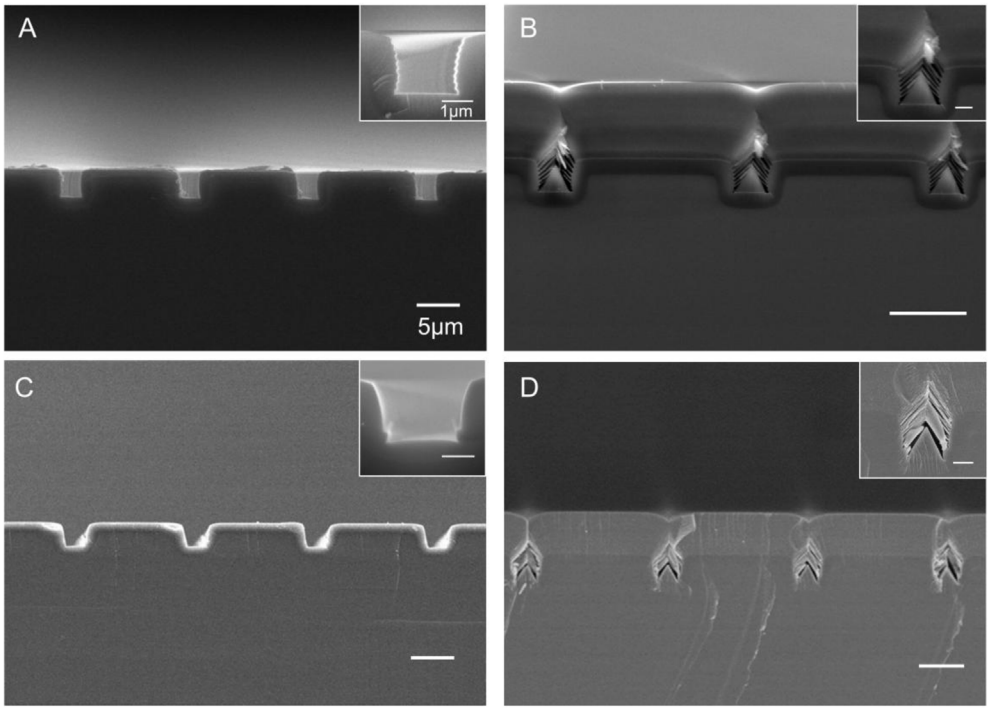

Fig. 2. SEM cross-sectional images of the separation channel array from a representative device. (A) Separation channel array prior to the deposition of nanorods. The scalloped edges are created through a custom DRIE process and serve as precursors for further growth of nanorods via shadowing effect (inset). (B) The channel array integrated with nanorod sieve featuring 200-nm pore aperture. (C) The channel array eliminates the taper scalloping with a smooth sidewall for nanorod sieve with high porosity. (D) The channel array integrated with nanorod sieve featuring sub-100 nm aperture. Scale bars: 5 μm. Scale bars in inset: 1 μm.

3.2. Long DNA sieving

We first evaluated the sieving performance of devices with 200-nm pore aperture for long DNA. A mixture of λ-DNA (48.5 kbp) and T4-DNA (166 kbp) was injected into a representative device with ten repeating trenches packed with nanorods (Fig. 3A). The obtained electrophoregrams at the detection point (5 mm from the injection cross-junction) were depicted in Fig. 3B. As can be seen, DNA molecules were

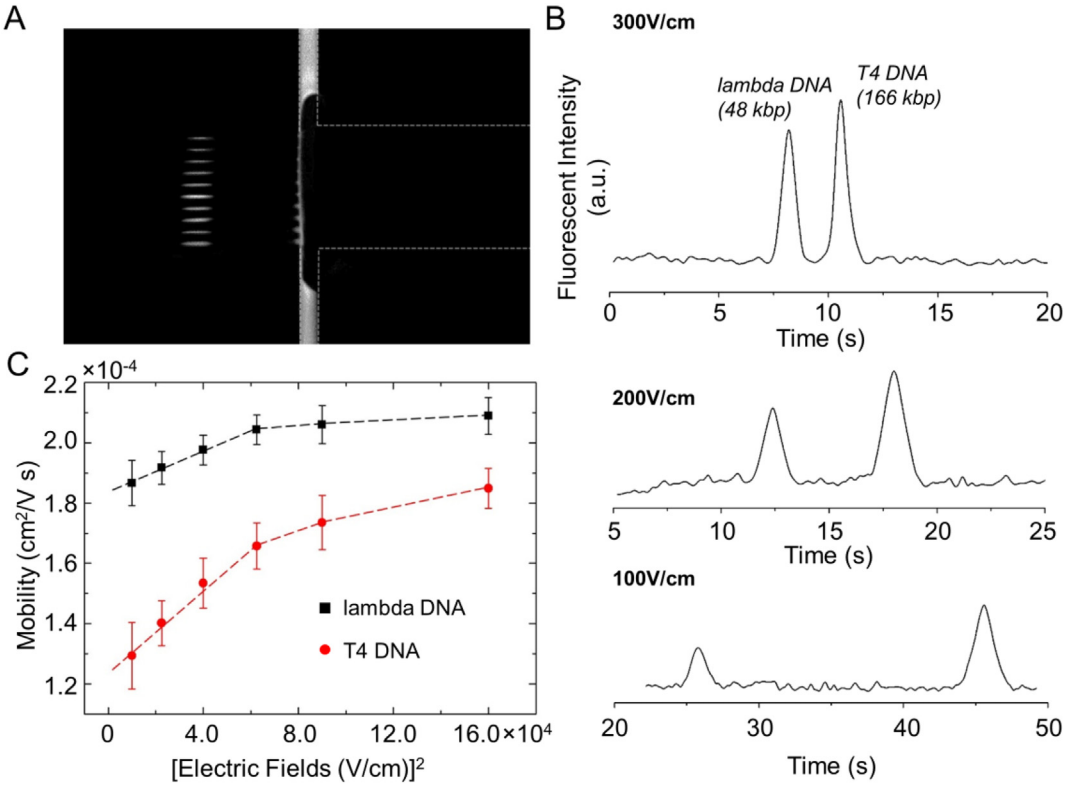

Fig. 3. Separation of long DNA molecules on nanorod sieve device with 200-nm pore aperture. (A) Fluorescence image showing the injection of DNA plug into the separation channel array. (B) Electropherograms obtained from the device with 1 cm separation length under varying electric field strengths. (C) The mobility of λDNA (black rectangles) and T4 DNA (red circles) as a function of the square of the applied electric field. The error bars indicate the standard errors of the respective mean values for five repetitious runs using the same device. (For interpretation of the references to colour in this figure legend, the reader is referred to the Web version of this article.)

Table 1
Experimentally obtained separation parameters at the end of a 5 mm-long separation channel under various field strength using nanorod sieve device with 200-nm pore aperture.

Voltage (V)	Theoretical plate number[a] × 10^3		Migration time (s)		Peak area × 10^4		Resolution[b]
	λDNA	T4	λDNA	T4	λDNA	T4	
150	0.9	1.3	8.2	10.6	3.0	3.3	2.1
100	1.0	2.5	12.4	18.0	2.2	4.0	3.7
50	2.5	4.8	25.8	45.6	1.6	4.0	8.4

[a] The theoretical plate number is evaluated based on $N = 16(t/W)^2$, which is the square of the ratio between the migration time and baseline width of a specific peak of interest.
[b] The resolution is calculated as $R_s = 2\Delta t/(W_1 + W_2)$, which is the distance between the two peaks scaled by their average width at base line.

fully resolved within 1 min under various field strength. The calculated separation parameters, including theoretical plate numbers, migration time, peak area and resolution, were summarized in Table 1. It was found that both theoretical plate numbers and resolution increased with the reduction of voltage. For instance, the sieving resolution improved from 2.1 to 8.4 as the voltage decreased from 150 V to 50 V, while the theoretical plate numbers of T4-DNA also rose from 1.3×10^3 to 4.8×10^3. The degradation of separation efficiency under high voltage arose from more Joule heat generated under intensified fields, which led to the band dispersion. The similar result was observed when high conductive buffer was used in our experiment. The electropherograms obtained were shown and compared in Fig. S1 (Supporting Information), where 2 × TBE buffer instead of 5 × TBE was used while preserving the same separation electric field. It was unveiled that the resolution improved from 2.1 to 3.2 as the concentration decreased, while the theoretical plate numbers of T4-DNA also increased from 1.3×10^3 to 1.9×10^3. The improved resolution under low voltage was attributed to the more interaction between DNA molecules and the nanorod sieves, which increased the size-dependent trapping time. Consequently, it may be desirable to run separation with lower electric field for higher resolution and plate numbers. Nevertheless, there was an evident slowdown of separation speed at a reduced field strength, which means a dramatically increased run time. As shown in Fig. 3B, the total separation proportionally increased from 10.6 s to 45.6 s in response to a 3-fold decrease in the field strength. A threshold voltage of 10 V over 5 mm was also observed in our device, under which the DNA band could not be launched into the nanorod sieve. Repeatability of the separation was also confirmed by five repetitious runs performed on one device subjected to the same conditions. The calculated percent relative standard deviation (RSD %) values were summarized in Table 2. The deviations were found to be relatively small (< 15%), which indicated a high reproducibility of the assay. To investigate the field dependence of mobility in nanorod sieves, we extracted the resultant mobility plots from the electrophoregrams as a function of the square of electric field (Fig. 3C). At a low field strength (< 300 V/cm), the mobility stays a linear trend with the square of electric field, which implies a biased reptation sieving mechanism where the deformation of DNA molecules occurs during their migration through the nanorod sieves. In this regime, the DNA molecules get stretched by the obstacles during their travel, and thus the mobility becomes more dependent on the electric force rather than on the length. The relation describing the regime is derived by Luckey and Smith as follows (Luckey and Smith, 1993):

$$\mu = \frac{Q}{\zeta}\left(\frac{(cE)^2}{9} + \frac{B}{N}\right) \quad (1)$$

where Q is the charge of DNA, ζ is friction coefficient for translational motion, cE is the dimensionless reduced electric field, B is a size-dependent constant and N is the DNA base pairs. It is noted that under the low electric field, the first term in eq. (1) tends to be zero. Therefore, the mobility of DNA is proportional to $1/N$, mainly determined by the DNA length instead of the field. On the contrary, the second term can be neglected under high field strength compared with the first term, registering the mobility independence of DNA size. As shown in Fig. 3C, the experimental data show excellent agreement with the fitting curves with $R^2 > 0.99$ at low field regime ($E < 300\ V/cm$). The curve deviates from the linear trend and reaches a plateau when the field exceeds 300 V/cm, which implies the model is no longer adequate at this condition. The mobility slope of T4 DNA is larger than that of λDNA, and these two curves level off and approach to the same maximum free mobility. This indicates our nanorod sieve would lose the size selectivity at high fields.

For negative control, additional channels without any nanorod sieves were examined for electrophoresis of mixture of λ-DNA and T4 DNA. Only one peak was detected under a broad range of voltage (Fig. S2, Supporting Information), which suggested both DNA fragments could not be resolved without the embedded nanorod sieves. The maximum sieving-free mobility was calculated as 2.2×10^{-4} $cm^2/(V\,s)$, which was correlated to the plateau of mobility curves (Fig. 3C) at high electric fields. Small DNA molecules ranging from 100 bp to 1000 bp were also evaluated and the electropherogram was obtained (Fig. S3, Supporting Information) using this 200-nm design with 2 cm separation length. The DNA molecules less than 400 bp were partially resolved and eluted first, while the peak eluted last contains all the large DNA molecules (500–1000 bp) that could not be separated. This was attributed to the less interaction and retardation due to the relatively smaller size of DNA fragments compared with sieving aperture.

Table 2
Percent relative standard deviation (RSD %) of separation parameters experimentally obtained from five repetitious runs using nanorod sieve device with 200-nm pore aperture.

Voltage (V)	RSD (%)					
	Migration time		Peak height		Peak area	
	λDNA	T4	λDNA	T4	λDNA	T4
150	4.9	7.7	5.7	6.3	8.7	8.1
100	5.2	8.4	7.5	8.4	9.5	10.2
50	8.3	8.6	10.8	10.3	12.2	11.8

3.3. Short DNA sieving

The resolving of short DNA molecules was achieved using nanorod sieve devices with small pore aperture. A mixture of 100 bp DNA ladder was separated in the nanorod sieve device that featured sub-100 nm pore aperture and 2 cm separation length. From the electrophorogram shown in Fig. 4A, the sample was separated into individual strands according to their size within 10 min under the voltage of 500 V across 2 cm length. The smaller DNA was eluted first with higher mobility. With a gyration radius (~75 nm for 1000-bp dsDNA) smaller than average pore aperture, the dominant separation mechanism was believed to be Ogston sieving. The elution order was confirmed by running the individual DNA strand separately in the device. The obtained

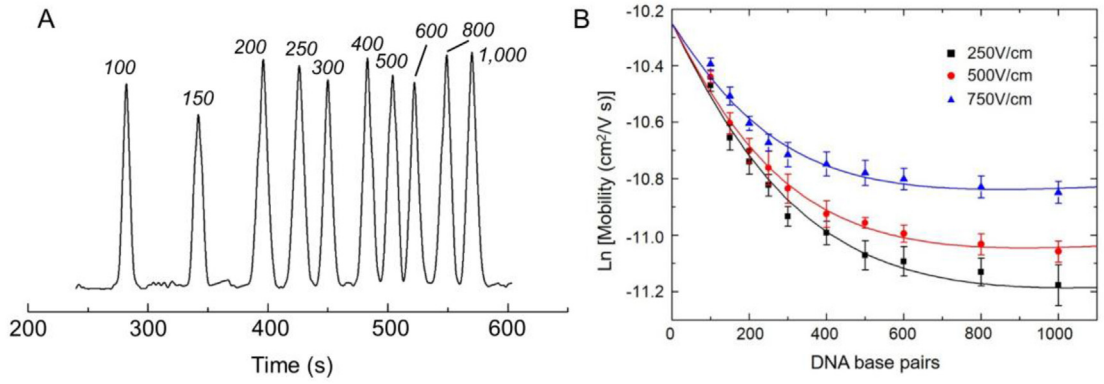

Fig. 4. (A) Electropherograms of 100-bp DNA ladder on the devices with 100-nm pore aperture and 2 cm separation length under the field of 250 V/cm. (B) The extracted mobility of DNA fragments as a function of chain length. The data is fitted with the curve based on eq. (3) with the parameter $a_1 = 5.51 \times 10^{-20}$ cm/V. The error bars indicate the standard errors of the respective mean values for five repetitious runs using the same device.

theoretical plate number was 2.5×10^3 for 1000 bp DNA ($\sim 1.25 \times 10^3\ m^{-1}$), an order of magnitude larger than that in the device with 200-nm pore aperture (Supporting Information, Table S1). The high efficiency achieved arose from the fact that dense arrays of nanorods could largely prevent the diffusion of molecules during their migration and therefore alleviate band dispersion. The resolving power of the sieve could be assessed using a minimum resolvable size difference R_M, which was defined as the ratio between the differential size of two peaks ΔM and the corresponding resolution R_s, *i.e.*, $R_M = \Delta M/R_s$. The resolution between 100 bp and 150 bp was assessed as 4.98, corresponding to a minimum resolvable size difference of 10 bp. In comparison, Fu et al. demonstrated a separation of a 100 bp DNA ladder using the 80-nm slit-well artificial sieves in 2.5 h under a field of 26 V/cm (Fu et al., 2006). The achieved R_M was calculated to be 67 bp between 800 and 900 bp DNA. Self-assembled colloidal arrays of silica beads by Zeng and Harrison were reported as a biomolecular sieving matrix with 56 bp R_M for 750 and 800 bp DNA (Zeng and Harrison, 2007). Cao et al. attained a R_M of 20 bp for 200 and 300 bp DNA using the capillary-well motif, which employed self-enclosed capillary arrays for sieving of 100-bp DNA ladder under high voltage (> 1000 V/cm) (Cao and Yobas, 2015).

The semilog plot of mobility against DNA size under different electric fields was illustrated in Fig. 4B. The smaller DNA fragments (< 300 bp) exhibited a fairly good linearity in the plot as predicted by Ogston model, where DNA was treated as a migrating spherical particle through fixed pores. In this condition, the mobility could be simply expressed as (Luckey and Smith, 1993):

$$\mu = \mu_0 \exp(-\alpha CN) \tag{2}$$

where μ_0 is the maximum free mobility without any sieves. α is a fitting parameter. C is a parameter dependent on the pore aperture. For the extremely small DNA fragment, $N \sim 0$, their mobility was nearly constant, $\mu \sim \mu_0$, which was independent of base pairs N and electric field E. The linear fitting of the data, for which the number of base pairs is lower than 300bp, at all three fields in Fig. 4B gives the intercept of y-axis a nearly constant value of -10.25, which corresponds to the free mobility $\mu_0 \sim 3.54 \times 10^{-5}$. For DNA larger than 300 bp, deviations from the linear relationship became apparent and the mobility was found to be significantly field-dependent. This could not be explicitly explained by classic Ogston model in eq. (1), which has no electric field term in the expression. Luckey et al. also found similar variations in mobility with regards to electric field strength (Luckey and Smith, 1993). They proposed a modification of the Ogston sieving theory which considered the stretching of migrating DNA molecules in the direction of the electric field and introduced a correction term to compensate the mobility. In this case, the mobility was expressed as

$$ln\mu = ln\mu_0 - \alpha CN\,[1 + [a_1 E]^{1/4} N^{3/2}]^{-1} \tag{3}$$

where a_1 is a constant independent of molecule size and fields. Excellent agreement with the experimental data was obtained for all the curves using the corrected model ($R^2 > 0.97$, Fig. 4B). The optimal fitting value of a_1 is 5.51×10^{-20} cm/V for all three curves, higher than 2.76×10^{-20} cm/V reported in agarose gel electrophoresis (Luckey and Smith, 1993). It should be noted that in eq (3), when $N > [2/(a_1 E)^{1/4}]^{2/3}$ ($\sim$900 bp for 250 V/cm), the mobility no longer monotonically decreased with the increase of DNA base pairs. Instead, larger DNA migrated faster than small DNA. This implied a cross-over from Ogston mechanism to reptation and the migration molecules could not maintain the spherical conformation through the sieves.

3.4. SDS-protein sieving

Proteins play critical roles in various biologically related activities, such as metabolic reactions, immune response and signal transmission between cells. The separation of proteins is of utmost importance for biomedicine and bioanalysis. The sieving of proteins requires much smaller pore aperture of matrix, which is challenging in device design. In this work, we have tested the utility of our sub-100 nm nanorod sieve in separating SDS-denatured proteins. An equimolar mixture of four SDS-denatured proteins, whose molecular weight ranges from 11.4 to 205 kDa, were successfully resolved into distinct peaks under 250 V/cm using the sieve featured sub-100 nm pore aperture and 2 cm channel length. As exhibited in Fig. 5A, the resolution between the 11.4 kDa and 68 kDa proteins was 7.22, achieving a minimum resolvable size difference R_M of 7.9 kDa, which is larger than the previous reported 7.8 kDa in capillary-well motif (Cao and Yobas, 2015) and 6.2 kDa using self-assembled colloidal arrays (Zeng and Harrison, 2007). The value of R_M gives an estimation on the smallest difference of proteins that could be well separated. Proteins with molecular weight difference below 7.9 kDa might not be fully resolved using our sieves. We confirmed this by conducting experiments using lectin GS-II (Griffonia simplicifolia, 113 kDa) and β-galactosidase (116 kDa). From the electropherograms shown in Fig. S4 (Supporting Information), these two proteins with the molecular weight difference 3 kDa could be hardly separated using our sieving matrix. We are now investigating the way to further scale down the pore aperture to improve the sieving capability. The theoretical plate numbers were 6.6–7.5 $\times 10^3$ ($\sim 10^5$ plates/m), an order of magnitude lower than 100-bp DNA ladder (Supporting Information, Table S2). This could be partly due to the pronounced interaction between protein molecules and the nanorod surfaces. Fig. 5B shows the logarithmic mobility of the proteins as a function of their molecular weight. The mean values were obtained from five repetitious runs performed on the same device. The RSD values were calculated from five repetitious runs on a single device (Supporting Information,

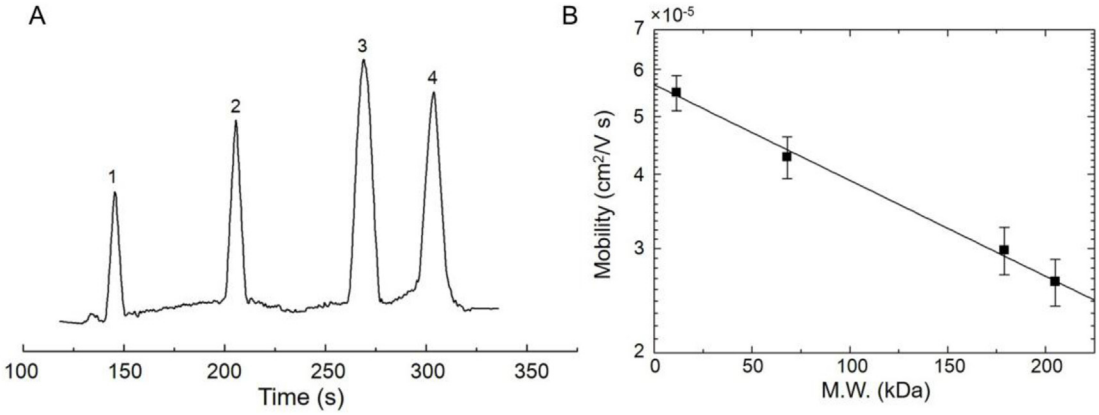

Fig. 5. (A) Electropherogram obtained from the device with sub-100 nm pore aperture and 2 cm long channel for separation of SDS-proteins under a field strength of 250 V/cm. The peaks are assigned as: (1) cholera toxin subunit B (11.4 kDa), (2) BSA (68 kDa), (3) human low-density lipoprotein (179 kDa), (4) myosin (205 kDa). (B) A semilog plot of the apparent mobility of SDS-proteins as a function of their molecular weight with a linear fit.

Table S3). The RSD values of the migration times, peak areas and resolutions were generally <10%, indicating an excellent repeatability of the separation. The data showed a good linearity with $R^2 > 0.99$, implying that Ogston mechanism mainly contributed to the separation of proteins.

3.5. Conclusions

We have demonstrated a novel sieving matrix, featuring integrated nanorod arrays, for high performance separation of biomolecules in a wide size range. Using this device, long DNA, short DNA and proteins could be separated into sharp peaks, either in the reptation mode or Ogston mechanism. The minimum resolvable size difference achieved is noted as 10 bp for 100 bp and 150 bp DNA fragments, 15.9 kbp for 48 kbp and 166 kbp DNA chains, and 7.9 kDa for 11.4 and 68 kDa proteins. By means of LOAD, nanorods are easily integrated into the separation channels of the sieving matrix, without the requirement of expensive nanofabrication tools. The density and the pore aperture of the matrix can be reliably controlled in favor of the sculptured edges of sidewalls created by a custom DRIE recipe. The nanorod sieve device provides an effective and sensitive way for biomolecules separation and poses great potentials in future applications of integrated bioanalysis system.

Declaration of interests

None.

Acknowledgements

This project was financially supported by the National Natural Science Foundation of China (Grant No. 61701438), General Research Fund HKBU 200813 of University Grants Committee in Hong Kong, and scientific research equipment development project of Chinese Academy of Sciences YZ201653.

Appendix A. Supplementary data

Supplementary data to this article can be found online at https://doi.org/10.1016/j.bios.2019.04.033.

References

Baba, M., Sano, T., Iguchi, N., Iida, K., Sakamoto, T., Kawaura, H., 2003. Appl. Phys. Lett. 83, 1468–1470.
Bakajin, O., Duke, T.A.J., Tegenfeldt, J., Chou, C.F., Chan, S.S., Austin, R.H., Cox, E.C., 2001. Anal. Chem. 73, 6053–6056.
Cao, Z., Yobas, L., 2014. Anal. Chem. 86, 737–743.
Cao, Z., Yobas, L., 2015. ACS Nano 9, 427–435.
Dorfman, K.D., 2010. Rev. Mod. Phys. 82, 2903–2947.
Duke, T.A.J., Austin, R.H., 1998. Phys. Rev. Lett. 80, 1552–1555.
Fu, J., Cao, Z., Yobas, L., 2011. Nanotechnology 22, 505302.
Fu, J.P., Mao, P., Han, J., 2008. Trends Biotechnol. 26, 311–320.
Fu, J.P., Mao, P., Han, J., 2005. Appl. Phys. Lett. 87, 263902.
Fu, J.P., Yoo, J., Han, J., 2006. Phys. Rev. Lett. 97, 018103.
Gao, F., Fan, T., Ou, S., Wu, J., Zhang, X., Luo, J., Li, N., Yao, Y., Mou, Y., Liao, X., Geng, D., 2018. Biosens. Bioelectron. 99, 201–208.
Gao, F., Fan, T., Wu, J., Liu, S., Du, Y., Yao, Y., Zhou, F., Zhang, Y., Liao, X., Geng, D., 2017. Biosens. Bioelectron. 96, 62–67.
Han, J., Craighead, H.G., 1999. J. Vac. Sci. Technol. A 17, 2142–2147.
Han, J., Craighead, H.G., 2000. Science 288, 1026–1029.
Han, J., Craighead, H.G., 2002. Anal. Chem. 74, 394–401.
Han, J., Turner, S.W., Craighead, H.G., 1999. Phys. Rev. Lett. 83, 1688–1691.
Huang, L.R., Cox, E.C., Austin, R.H., Sturm, J.C., 2003. Anal. Chem. 75, 6963–6967.
Huang, L.R., Tegenfeldt, J.O., Kraeft, J.J., Sturm, J.C., Austin, R.H., Cox, E.C., 2002. Nat. Biotechnol. 20, 1048–1051.
Ji, X., Xiao, C., Lau, W.F., Li, J., Fu, J., 2016. Biosens. Bioelectron. 82, 240–247.
Kaji, N., Tezuka, Y., Takamura, Y., Ueda, M., Nishimoto, T., Nakanishi, H., Horiike, Y., Baba, Y., 2004. Anal. Chem. 76, 15–22.
Lee, H.J., Hwang, N.R., Hwang, S.H., Cho, Y., 2016. Biosens. Bioelectron. 86, 864–870.
Liu, J., Shirota, O., Novotny, M.V., 1992. Anal. Chem. 64, 973–975.
Luckey, J.A., Smith, L.M., 1993. Electrophoresis 14, 492–501.
Ma, C., Wang, W., Yang, Q., Shi, C., Cao, L., 2011. Biosens. Bioelectron. 26, 3309–3312.
Qian, Y., Fan, T., Yao, Y., Shi, X., Liao, X., Zhou, F., Gao, F., 2018. Sensor. Actuator. B Chem. 254, 483–489.
Rahong, S., Yasui, T., Yanagida, T., Nagashima, K., Kanai, M., Meng, G., He, Y., Zhuge, F., Kaji, N., Kawai, T., 2015. Sci. Rep. 5, 10584.
Smejkal, G.B., Lazarev, A., 2006. Separation Methods in Proteomics. CRC Press, FL.
Stellwagen, N.C., 2009. Electrophoresis 30, S188–S195.
Viovy, J.-L., 2000. Rev. Mod. Phys. 72, 813.
Viovy, J.-L., Duke, T., 1993. Electrophoresis 14, 322–329.
Volkmuth, W.D., Austin, R.H., 1992. Nature 358, 600–602.
Wang, X., Veerappan, V., Cheng, C., Jiang, X., Allen, R.D., Dasgupta, P.K., Liu, S., 2010. J. Am. Chem. Soc. 132, 40–41.
Wang, X., Wang, S., Veerappan, V., Byun, C.K., Nguyen, H., Gendhar, B., Allen, R.D., Liu, S., 2008. Anal. Chem. 80, 5583–5589.
Westermeier, R., 2016. Electrophoresis in Practice: a Guide to Methods and Applications of DNA and Protein Separations. John Wiley & Sons, New York.
Wunsch, B.H., Kim, S.C., Gifford, S.M., Astier, Y., Wang, C., Bruce, R.L., Patel, J.V., Duch, E.A., Dawes, S., Stolovitzky, G., Smith, J.T., 2019. Lab Chip. https://doi.org/10.1039/C8LC01408F.
Wunsch, B.H., Smith, J.T., Gifford, S.M., Wang, C., Brink, M., Bruce, R.L., Austin, R.H., Stolovitzky, G., Astier, Y., 2016. Nat. Nanotechnol. 11, 936–940.
Yasui, T., Kaji, N., Ogawa, R., Hashioka, S., Tokeshi, M., Horiike, Y., Baba, Y., 2011. Anal. Chem. 83, 6635–6640.
Zeming, K.K., Salafi, T., Shikha, S., Zhang, Y., 2018. Nat. Commun. 9, 1254.
Zeng, Y., Harrison, D.J., 2007. Anal. Chem. 79, 2289–2295.
Zhang, M., Cao, Z., Yobas, L., 2013. Sensor. Actuator. B Chem. 184, 235–242.
Zhu, Z., Liu, L., Wang, W., Lu, J.J., Wang, X., Liu, S., 2013. Chem. Commun. 49, 2897–2899.